


Article

Beryllium Dimer Reactions with Acetonitrile: Formation of Strong Be–Be Bonds

Fei Cong ¹, Liyan Cai ¹, Juanjuan Cheng ¹, Zhen Pu ^{2,*} and Xuefeng Wang ^{1,*} 

¹ Shanghai Key Lab of Chemical Assessment and Sustainability, School of Chemical Science and Engineering, Tongji University, Shanghai 200092, China; 1810918@tongji.edu.cn (F.C.); 2110184@tongji.edu.cn (L.C.); chengjuanjuan@tongji.edu.cn (J.C.)

² China Academy of Engineering and Physics, Mianyang 621900, China

* Correspondence: puzhen@caep.cn (Z.P.); xfwang@tongji.edu.cn (X.W.)

Abstract: Laser ablated Be atoms have been reacted with acetonitrile molecules in 4 K solid neon matrix. The diberyllium products BeBeNCCH₃ and CNBeBeCH₃ have been identified by D and ¹³C isotopic substitutions and quantum chemical calculations. The stabilization of the diberyllium species is rationalized from the formation of the real Be–Be single bonds with bond distances as 2.077 and 2.058 Å and binding energies as −27.1 and −77.2 kcal/mol calculated at CCSD (T)/aug-cc-pVTZ level of theory for BeBeNCCH₃ and CNBeBeCH₃, respectively. EDA-NOCV analysis described the interaction between Be₂ and NC⋯CH₃ fragments as Lewis “acid–base” interactions. In the complexes, the Be₂ moiety carries positive charges which transfer from antibonding orbital of Be₂ to the bonding fragments significantly strengthen the Be–Be bonds that are corroborated by AIM, LOL and NBO analyses. In addition, mono beryllium products BeNCCH₃, CNBeCH₃, HBeCH₂CN and HBeNCCH₂ have also been observed in our experiments.

Keywords: Be–Be bonds; beryllium dimer; infrared spectrum; quantum chemical calculations



Citation: Cong, F.; Cai, L.; Cheng, J.; Pu, Z.; Wang, X. Beryllium Dimer Reactions with Acetonitrile: Formation of Strong Be–Be Bonds. *Molecules* **2024**, *29*, 177. <https://doi.org/10.3390/molecules29010177>

Academic Editor: Ángel Martín Pendás

Received: 11 November 2023

Revised: 25 December 2023

Accepted: 26 December 2023

Published: 28 December 2023



Copyright: © 2023 by the authors. Licensee MDPI, Basel, Switzerland. This article is an open access article distributed under the terms and conditions of the Creative Commons Attribution (CC BY) license (<https://creativecommons.org/licenses/by/4.0/>).

1. Introduction

The chemistry of beryllium is predicted to be the richest among the alkaline earth metals due to its small size and the highest electronegativity and ionization energy among *s*-block elements [1,2], which is, however, largely unexplored due to the high toxicity of the compounds containing this element [3,4]. Over the past few decades, the very weak beryllium–beryllium interaction has been the most studied for *s*-block metal–metal interactions [5–7]. Isolated beryllium dimer was characterized as a typical weakly bound molecule with a bonding interaction of 11.2 kJ mol^{−1} (calc.) and a large bond distance of 2.45 Å as a result of the both doubly occupied bonding 2σ_g⁺ orbital and antibonding 2σ_u⁺ orbital [8–10].

Up to now, diberyllium complexes have aroused a great deal of enthusiasm among researchers, and many theoretical strategies have been proposed to enhance the strength of Be–Be bond [5,11–15]. Removing/adding an electron from/to this dimer by interaction with some other molecules is a general formula to stabilize the system. The complexation of Be₂ with electron-withdrawing ligands such as F [16] or CN [17], or electron-deficient conjugated fragments such as cyclopentadienyl [18,19], pentadienyl [20] and phospholyl [21] is able to obtain a classical Be–Be σ single bond by pulling one or both electrons from antibonding orbital of Be₂ to ligands. Despite the intrinsic electron-deficient nature of beryllium, reports indicate that the Be₂ moiety in these molecules is essentially a dication Be₂²⁺, [17] which exhibits the formation of a strong bond in the presence of a counterion. Strong Be–Be bonds are also formed via electron transferring from Be atoms to C_nH_n (n = 3, 5, 7), π-radicals [22] and SO ligands. [23] Furthermore, a neutral odd-electron Be–Be bond is firstly identified in the tri-AMD-ligands-chelated D_{3h}-Be₂(AMD)₃ complex by one

AMD ligand attracting one electron from Be antibonding σ^* orbital [24]. A strong 2-center-1-electron Be–Be bond is also formed by attaching one electron to 1,2-diBeX-benzene ($X = H, F, Cl, CN$) derivatives [25]. Be–Be double- π bonds are first achieved in the predicted octahedral cluster of $Be_2(\mu_2-X)_4$ ($X = Li, Cu, BeF$) by a novel concerted electron-donation from four s^1 -type electron-donating ligands [15]. The Be–Be triple bonds are formed in theoretically predicted Li_6Be_2 [26] species, which are stabilized by six s^1 -type donor ligands and in $Be_2X_4Y_2$ ($X = Li, Na; Y = Na, K$) [27] clusters where six alkali metals are electron-donating ligands. Another way to form a Be–Be covalent bond is by adding radical ligands to an excited Be_2 moiety. The neutral Be_2 moiety in an excited state adding ligands such as $(HCNMe)_2B$ [28] and *N*-heterocyclic carbenes (NHCs) [29] can form a single or double bond, respectively.

Acetonitrile is known as an effective electron donor based on the previous research of reactions with metal atoms [30–37], and it could be a good candidate for stabilizing the Be_2 dimer. In this paper, we investigated the reactions of beryllium atoms with acetonitrile by means of matrix-isolation infrared spectroscopy and theoretical calculations, in order to further supplement the reactions of alkali metal with acetonitrile, and search for stable diberyllium complexes that might be formed. Six different products were spectroscopically identified in solid neon including two complexes possessing Be–Be single bonds, and three related reaction paths were presented.

2. Results and Discussion

The infrared spectra for acetonitrile (0.5% in solid neon) on pre-deposition and the reaction products on co-deposition, annealing and stepwise photolysis in the selected regions are shown in Figure 1. The isotopic substitution experiments with CD_3CN and $^{13}CH_3^{13}CN$ samples were performed and the infrared spectra are given in Figure 2. The absorptions of acetonitrile are extremely strong, so the changes of acetonitrile absorptions during the reaction are negligible compared with the products' absorptions. In addition to the absorptions assigned to the precursor and common species that were also observed in other experiments with CH_3CN as reagent, several new product absorptions appeared, which can be classified into six groups based on their intensity changes. Table 1 shows the observed and computed vibrational frequencies of the products along with the assignment of the modes. The full sets of B3LYP calculated harmonic and anharmonic frequencies are all collected in Tables S1–S6. The laser intensity is relatively high in our experiments that are able to directly produce beryllium dimer. The infrared intensities of diberyllium products are much weaker with low laser power, while the intensities of mono beryllium products almost remain unchanged in Figure 1a. Several new absorptions located in N–C and C–N stretching region are almost diminished with low laser intensity. We tentatively assigned these weak absorptions to $Be_x(CH_3CN)$, which were generated from the reactions of Be clusters and acetonitrile with high laser power.

The relatively weak absorptions in the original deposition spectra marked “1” were completely destroyed under visible irradiation. New product absorptions denoted with “2” also appeared upon sample deposition, which decreased after annealing to 8 K and totally disappeared on the first visible ($\lambda = 520$ nm) irradiation. On the opposite, the intensities of the bands marked with “3” and “4” tripled and doubled upon full arc irradiation ($\lambda > 220$ nm) compared with the co-deposition spectra. In addition, the relatively weak absorptions marked “5” and “6” only appeared after full arc irradiation.

2.1. End-On Products: $BeBeNCCH_3$ and $BeNCCH_3$

The absorption of C–N stretching mode for $BeBeNCCH_3$ complex was observed at 1927.8 cm^{-1} on co-deposition, and its corresponding ^{13}C counterpart was located at 1889.4 cm^{-1} , but unfortunately the corresponding D isotopic absorption was covered by the precursor bands. The observed absorptions matched well with the computed IR frequencies with strongest intensities at 1986.0 and 1942.7 cm^{-1} for ^{12}C and ^{13}C , respectively. The band at 994.1 cm^{-1} is attributed to the CH_3 bending mode, with D and ^{13}C counterparts observed

at 827.0 and 981.2 cm^{-1} , respectively. The computed infrared absorptions of BeBeNCCH_3 are shown in Table S1.

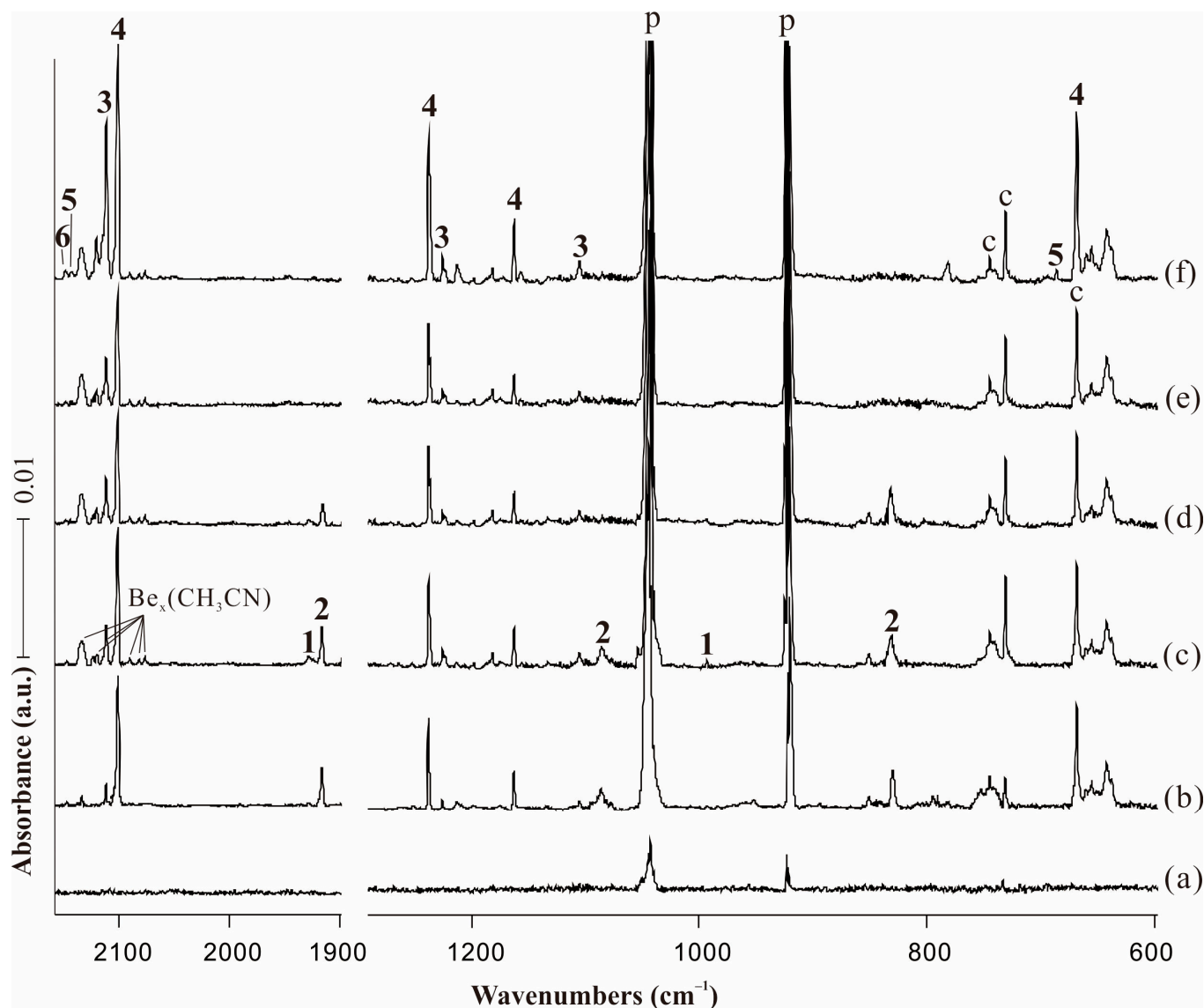


Figure 1. Infrared spectra in the product regions from the reactions of laser-ablated Be atoms with 0.5% CH_3CN in neon matrix at 4 K. (a) Pre-deposition of 0.5% CH_3CN in neon for 6 min; (b) co-deposition for 60 min (weaker laser intensity); (c) co-deposition for 60 min (higher laser intensity); (d) after annealing at 8 K; (e) after visible ($\lambda > 520$ nm) irradiation for 6 min; and (f) after full arc ($\lambda > 220$ nm) irradiation for 6 min. Bands labeled p and c stand for the precursor absorptions and common absorptions in the CH_3CN matrix spectra. Numbers 1, 2, 3, 4, 5, 6 denote BeBeNCCH_3 , BeNCCH_3 , CNBeBeCH_3 , CNBeCH_3 , HBeCH_2CN and HBeNCCH_2 , respectively.

The assignment of the mono beryllium end-on complex BeNCCH_3 was confirmed by the experimental observation of three bands at 1915.4, 1082.3 and 831.4 cm^{-1} . The strong 1915.4 cm^{-1} band showed a large ^{13}C shift to 1875.4 cm^{-1} , exhibiting a $^{12}\text{C}/^{13}\text{C}$ isotopic frequency ratio of 1.0213, while its corresponding D counterpart was at 1911.2 cm^{-1} . We assigned this band to the C–N stretching mode of BeNCCH_3 based on the isotopic shifts and good consistence with the calculated value of 1953.5 cm^{-1} . The bands at 1082.3, 1020.8 and 1068.7 cm^{-1} for ^{12}C , D and ^{13}C isotopes are in good agreement with the calculated results of N–Be stretching mode at 1106.0 (^{12}C), 1043.4 (D) and 1091.5 cm^{-1} (^{13}C), respectively. The absorption observed at 831.4 cm^{-1} with a ^{13}C isotopic substitution at 811.6 cm^{-1} lays

in the region expected for a C–C stretching vibration, [37] and the large $^{12}\text{C}/^{13}\text{C}$ ratio of 1.0244 was obtained to verify our assignment. The corresponding D isotopic absorption was covered by the precursor bands. All calculated frequencies of BeNCCH_3 are listed in Table S2.

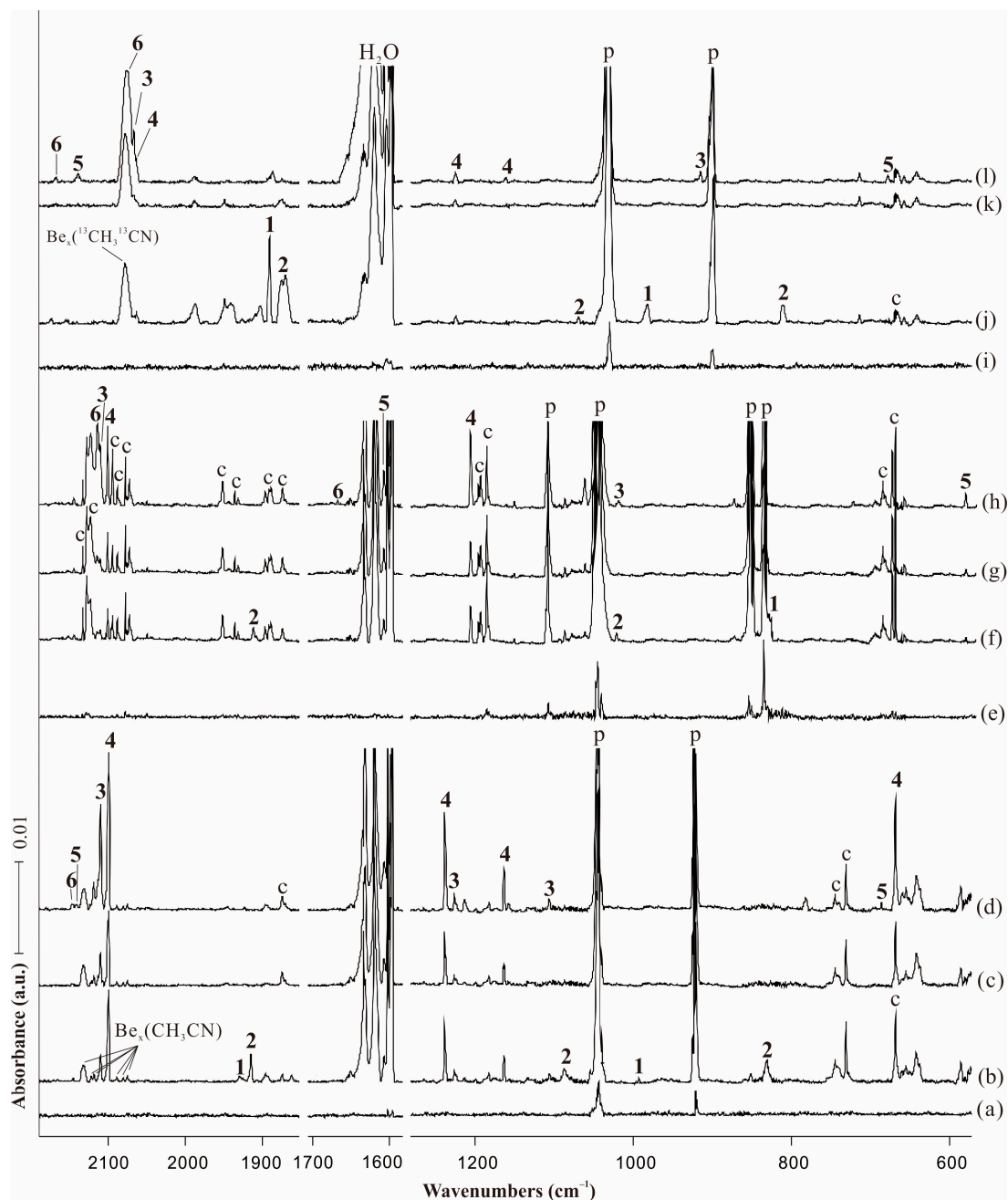


Figure 2. Infrared spectra in the product regions from the reactions of laser-ablated Be atoms with CH_3CN in neon matrix at 4 K. (a) Pre-deposition of 0.5% CH_3CN in neon for 6 min; (b) co-deposition of Be + 0.5% CH_3CN for 60 min; (c) after visible ($\lambda = 520$ nm) irradiation; (d) after full arc ($\lambda > 220$ nm) irradiation for 6 min; (e) pre-deposition of 0.75% CD_3CN in neon for 6 min; (f) co-deposition of Be + 0.75% CD_3CN for 60 min; (g) after visible ($\lambda = 520$ nm) irradiation; (h) after full arc ($\lambda > 220$ nm) irradiation for 6 min; (i) pre-deposition of 0.75% $^{13}\text{CH}_3^{13}\text{CN}$ in neon for 6 min; (j) co-deposition of Be + 0.75% $^{13}\text{CH}_3^{13}\text{CN}$ for 60 min; (k) after visible ($\lambda = 520$ nm) irradiation; and (l) after full arc ($\lambda > 220$ nm) irradiation for 6 min. Bands labeled p and c stand for the precursor absorptions and common absorptions in the CH_3CN matrix spectra. Numbers 1, 2, 3, 4, 5, 6 denote BeBeNCCH_3 , BeNCCH_3 , CNBeBeCH_3 , CNBeCH_3 , HBeCH_2CN and HBeNCCH_2 , respectively.

Table 1. Experimentally observed (in Ne) and calculated vibrational frequencies of products from reactions of beryllium atoms with acetonitrile ^a.

Be + CH ₃ CN		Be + CD ₃ CN		Be + ¹³ CH ₃ ¹³ CN		Mode
Obs.	Cal.	Obs.	Cal.	Obs.	Cal.	
1927.8	1986.0 (1132)	covered ^b	1. BeBeNCCH ₃ 1984.3 (1151)	1889.4	1942.7 (1098)	C–N str.
994.1	986.0 (581)		812.3 (754)	981.2	975.1 (504)	CH ₃ bend
1915.4	1953.5 (119)	1911.2	2. BeNCCH ₃ 1952.1 (124)	1875.4	1915.6 (121)	C–N str.
1082.3	1106.0 (76)	1020.8	1043.4 (77)	1068.7	1091.5 (79)	N–Be str.
831.4	807.0 (71)	covered ^b	875.8 (82)	811.6	790.0 (67)	C–C str.
2111.0	2157.7 (458)	2111.9	3. CNBeBeCH ₃ 2157.7 (458)	2068.1	2117.7 (458)	N–C str.
1226.1	1249.1 (48)		1037.2 (3)		1237.2 (44)	CH ₃ wag
1105.6	1109.8 (44)		831.2 (56)		1105.9 (39)	Be–Be str.
Covered ^b	909.5 (185)	1013.4	1004.5 (212)	913.4	902.2 (185)	C–Be str.
2100.2	2164.8 (436)	2101.4	4. CNBeCH ₃ 2165.0 (428)	2064.3	2125.0 (438)	N–C str.
1237.8	1269.2 (160)	1205.0	1217.9 (301)	1223.8	1255.5 (146)	CH ₃ wag
1162.9	1186.4 (147)		951.4 (0)	1160.5	1183.2 (152)	CBeN as. str.
668.3	695.6 (88)		576.0 (83)		590.5 (87)	CBeN bend
2141.4	2196.1 (159)	1608.3	5. HBeCH ₂ CN 1654.6 (121)	2141.8	2195.9 (160)	Be–H str.
685.9	710.2 (139)	579.9	596.8 (96)	680.6	703.2 (141)	Be–H bend
2147.7	2204.0 (1309)	2114.6	6. HBeNCCH ₂ 2171.9 (1129)	2075.7	2197.2 (590)	C–N str.
	2179.9 (287)	1661.8	1688.5 (232)	2169.0	2129.1 (966)	Be–H str.

^a All frequencies are in cm^{−1} and the calculated IR intensities are in the parentheses (km mol^{−1}). The computed frequencies are given at the B3LYP–D3/aug–cc–pVTZ level of theory. ^b Absorptions covered by precursor bands.

2.2. Insertion Products: CNBeBeCH₃ and CNBeCH₃

The strong band at 2111.0 cm^{−1} is due to the N–C stretching vibration for the diberyllium insertion product CNBeBeCH₃, and the D and ¹³C isotopic substitutions were observed at 2111.9 and 2068.1 cm^{−1}, respectively, conforming to the N–C stretching mode shifts. The low-intensity band of CH₃ wagging mode is located at 1226.1 cm^{−1}, the predicted value of which is at 1249.1 cm^{−1}. The most decisive band for the diberyllium insertion product was observed at 1105.6 cm^{−1}, which matched well with the calculated absorption for Be–Be stretching mode at 1109.8 cm^{−1}. Unfortunately, the isotopic counterparts for these two absorptions were too weak to be observed in our experiments. The C–Be stretching mode was observed at 1013.4 and 913.4 cm^{−1} in D and ¹³C spectra, but this mode was covered by the extremely strong precursor absorption in ¹²C experiments.

The most intense absorption at 2100.2 cm^{−1} in the spectrum after full arc irradiation showed essentially no shift upon D substitution, but largely shifted to 2064.3 cm^{−1} on ¹³C. The B3LYP isotope ratio for ¹³C substitution of 1.0187 was in accordance with the experimental ratio of 1.0174. We therefore assigned the uniquely strong 2100.2 cm^{−1} band to the N–C stretching vibration of the mono beryllium insertion complex. The strong CH₃ wagging absorption observed at 1237.8 cm^{−1} showed its D and ¹³C isotopic absorptions at 1205.0 and 1223.8 cm^{−1}, and these bands are in excellent consistence with calculated values of 1269.2, 1217.9 and 1255.5 cm^{−1}, respectively. A medium absorption was observed at 1162.9 cm^{−1} along with its ¹³C counterpart at 1160.5 cm^{−1}, and it is indicative of the antisymmetric CBeN stretching vibration. The observed bands are in the good agreement with the calculated frequencies of 1186.4 and 1183.2 cm^{−1} for ¹²C and ¹³C isotopes. Though the band at 668.3 cm^{−1} is common in the matrix spectra of CH₃CN + M reactions, it only doubled under full arc irradiation in the case of beryllium, and tracked with other bands

labeled “4”. Unfortunately, its D and ^{13}C counterparts were not detected because of our detector noise. We tentatively assigned this band to the CBeN bending mode of CNBeCH_3 . The B3LYP functional predicted this band at 695.6 cm^{-1} , which is only 27.3 cm^{-1} higher than observed. The other infrared absorptions of CNBeCH_3 are very weak, which are not observed in the experiment (Table S4).

2.3. HBeCH_2CN and HBeNCCH_2

The band at 2141.4 cm^{-1} only appeared after full arc irradiation showing almost no ^{13}C shift at 2141.8 cm^{-1} . The Be–D stretching mode of HBeCH_2CN was calculated at 1654.6 cm^{-1} , and was observed at 1608.3 cm^{-1} among the strong absorptions of water impurity existing in all our experiments. We assigned these bands to the Be–H stretching mode of HBeCH_2CN . In the low frequency region, a weak absorption at 685.9 cm^{-1} tracked with 2141.1 cm^{-1} band, and it showed a large D shift to 579.9 cm^{-1} and very small ^{13}C shift to 680.6 cm^{-1} . The band position and large D shift of 106.0 cm^{-1} suggested a Be–H bending vibration. The observed bands are in excellent agreement with the calculated frequencies of 710.2 , 596.8 and 703.2 cm^{-1} , respectively. The observation of the Be–H bending mode overwhelmingly confirmed our assignment of HBeCH_2CN .

The band at 2147.7 cm^{-1} exhibited its D and ^{13}C counterparts at 2114.6 and 2075.7 cm^{-1} . The B3LYP computed $^{12}\text{C}/^{13}\text{C}$ isotopic frequency ratios for C–N stretching mode of HBeNCCH_2 was 1.0352, very slightly lower than the observed value of 1.0347. For D counterpart, the calculation result showed that the C–N stretching mode is coupled with CD_2 symmetric stretching vibration, which is the reason of the large D shift observed in the experiment. The coincident coupled frequency in D substitution is decisive for the confirmation of product HBeNCCH_2 . The Be–H stretching mode was observed at 1661.8 and 2169.0 cm^{-1} for D and ^{13}C , and the predicted values were at 1688.5 and 2197.2 cm^{-1} , respectively. The calculated intensities of the other infrared bands are all weak in Table S6.

3. Molecular Structures and Bonding

The optimized structures of diberyllium and mono beryllium end-on and insertion complexes are shown in Figure 3, with the end-on products in C_s symmetry and the insertion complexes possessing C_{3v} symmetry. The point groups of beryllium products happen to be reverse with the C_{3v} point groups of N-coordination transition-metal complexes and C_s structures of transition-metal insertion complexes (except for Mn products) [30–37]. According to the NBO analysis in Table S8, the electropositive beryllium forms sp hybrid orbitals, which make σ bonds with sp hybrid orbitals on the C atoms in the insertion complexes. The higher s contributions from Be in the C–Be bond lead to the linear structures, different from the higher d characters in the carbon–metal bond leading to the bent transition-metal structures. The unpaired spin destinies of triplet state BeNCCH_3 complex are most located on Be and C atoms (1.105 and 0.555, shown in Figure S1), which cause a bent structure with CCN bond angles of 134.6° .

Unlike the tiny differences in the structures, the diberyllium products are much more exothermic compared with mono beryllium complexes, which may be caused by the formation of the Be–Be real single bonds. The binding energies of the Be–Be bonds in BeBeNCCH_3 and CNBeBeCH_3 are calculated to be -27.1 and -77.2 kcal/mol at CCSD(T)/aug-cc-pVTZ level of theory, respectively. The Be–Be bond in CNBeBeCH_3 is also quantified by the EDA, as shown in Figure 4 and Table S9. The total interaction energy ΔE_{int} is $-73.72\text{ kcal}\cdot\text{mol}^{-1}$ between the NCB_e and BeCH₃ fragments, which consist of $-65.54\text{ kcal}\cdot\text{mol}^{-1}$ of electrostatic energy ΔE_{elstat} , $-41.61\text{ kcal}\cdot\text{mol}^{-1}$ of orbital interaction energy ΔE_{orb} , and $33.43\text{ kcal}\cdot\text{mol}^{-1}$ of Pauli repulsion energy ΔE_{Pauli} . For BeBeNCCH_3 , the Be–Be bond distance is calculated to be 2.077 \AA , significantly shorter than that in the free Be_2 dimer of 2.509 \AA . The Be–Be distance is further shortened in CNBeBeCH_3 with 2.058 \AA . The Be–Be distances match the single bond value of 2.05 \AA in reported calculations of comparable compounds, and the bond lengths are also closer to that of Be_2^{2+} than to the neutral Be_2 molecule [17]. Furthermore, the CN and CH₃ moieties are both doubly

occupied rather than singly occupied in HOMO-2 and HOMO-3 (Figure S2), which also indicates charge transfer from Be₂ to the bonding fragments. As expected, the beryllium atoms in our diberyllium products carry positive charge and the NC and CH₃ moieties are negatively charged. According to the NPA charges showed in Figure 3, the Be₂ moiety carries positive charges of 0.38 and 1.32 for BeBeNCCH₃ and CNBeBeCH₃, respectively. More positive charges on the Be₂ moiety lead to shorter Be–Be bond distances.

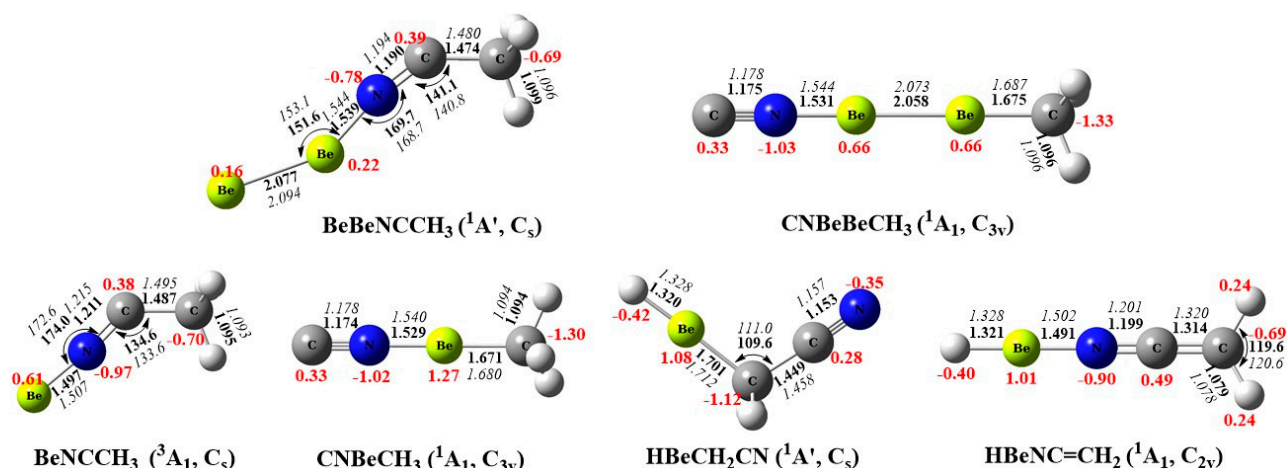


Figure 3. Optimized structures of the reaction products at the B3LYP–D3 (**bold**) and CCSD (*italic*) levels. The aug–cc–pVTZ basis was set for all atoms. Black color: bond length in Å and bond angle in degree; red color: the atomic partial charges calculated by the NBO method.

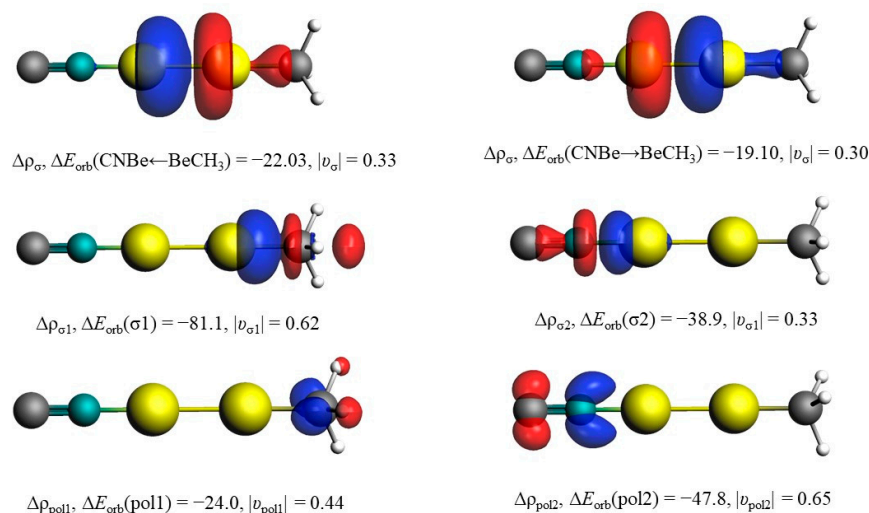


Figure 4. Plots of the deformation densities $\Delta\rho$. ΔE_{orb} are in kcal mol^{−1}. The direction of the charge flow is red → blue.

The energy decomposition analysis (EDA) in combination with the natural orbital for chemical valence (NOCV) theory has been carried out to further confirm the types of bonding in Table 2. There are two possibilities of interaction types in CNBeBeCH₃: ionic or neutral interacting fragments. The most suitable fragments to describe the bonding situations yield the smallest amount of the orbital interaction energy (ΔE_{orb}), because the least alteration of the electronic charge distribution is required to generate the electronic structure of the molecule. The significantly smaller ΔE_{orb} value of ionic fragments (by 183.7 kcal/mol) convincingly shows that CNBeBeCH₃ complex can be envisaged as the result of the interaction of Be₂²⁺ and (NC...CH₃)^{2−} through a donor–acceptor type of bonding rather than the electron-shared bonding between the neutral ones. The substantial

electrostatic energy ΔE_{elstat} (-640.7 kcal/mol) between the ionic interacting fragments contributes much more (75.9%) to the total attraction than the covalent contribution ΔE_{orb} (24.0%). The polarization interaction caused by strong electrostatic interaction is also not neglectable. The corresponding deformation densities $\Delta\rho$ due to the electron transfer between the ionic interacting fragments are visualized in Figure 4. The direction of the charge flow is from the red region to the blue one. The colors also corroborate well with the NPA charges in Figure 3. It is obvious that the orbital interactions in CNBeBeCH_3 are mainly σ donations of the Lewis base $(\text{NC}\cdots\text{CH}_3)^{2-}$ to the vacant σ_u^+ orbitals of the Lewis acid Be_2^{2+} .

Table 2. EDA-NOCV results for CNBeBeCH_3 obtained at the B3LYP/TZ2P/ZORA level of theory.

Energy Term ^a	Orbital Interaction	$\text{Be}_2^{2+} + (\text{H}_3\text{C}\cdots\text{NC})^{2-}$	$\text{Be}_2 + \text{H}_3\text{C}\cdots\text{NC}$
ΔE_{int}	-	-687.9	-252.5
ΔE_{Pauli}	-	155.7	414.4
$\Delta E_{\text{elstat}}^b$	-	-640.7 (75.9%)	-280.2 (42.0%)
ΔE_{orb}^b	-	-202.9 (24.0%)	-386.6 (58.0%)
$\Delta E_{\text{orb}}(\sigma_1)^c$	$\text{Be}_2^{2+} \leftarrow (\text{CH}_3)^-$ σ -donation	-81.1 (40.0%)	-
$\Delta E_{\text{orb}}(\sigma_2)^c$	$\text{Be}_2^{2+} \leftarrow (\text{NC})^-$ σ -donation	-38.9 (19.2%)	-
$\Delta E_{\text{orb}}(\text{pol}_1)^c$	$\text{H} \rightarrow \text{C}$ polarization	-24.0 (11.8%)	-
$\Delta E_{\text{orb}}(\text{pol}_2)^c$	$\text{C} \rightarrow \text{N}$ polarization	-47.8 (23.6%)	-26.2 (6.8%)
$\Delta E_{\text{orb}}(\sigma_3)^c$	$\text{Be}_2 \rightarrow \text{NC}$ σ -backdonation	-	-201.0 (52.0%)
$\Delta E_{\text{orb}}(\sigma_4)^c$	$\text{Be}_2 \rightarrow \text{CH}_3$ σ -backdonation	-	-105.5 (27.3%)
$\Delta E_{\text{orb}}(\sigma_5)^c$	$\text{Be}_2 \leftarrow \text{CH}_3$ σ -donation	-	-17.7 (4.6%)
$\Delta E_{\text{orb}}(\sigma_6)^c$	$\text{Be}_2 \leftarrow \text{CH}_3$ σ -donation	-	-24.9 (6.4%)
$\Delta E_{\text{orb}}(\text{rest})^c$	-	-11.1 (5.5%)	-11.3 (2.9%)
ΔE_{prep}	-	60.3	24.2
$\Delta E (-D_e)$	-	-627.6	-228.3

^a Energy values are given in kcal/mol. ^b The percentage contribution to the total attractive interactions ($\Delta E_{\text{elstat}} + \Delta E_{\text{orb}} + \Delta E_{\text{disp}}$) is given in parentheses. ^c The percentage contribution to the total orbital interactions is given in parentheses.

We also studied the topological analysis of electron density in these complexes to obtain a better understanding of the bonding situation. Figure 5 and Figure S3 display the contour plots of Laplacian of electron density ($\nabla^2\rho(r)$) at the molecular plane. The red dotted lines correspond to the areas of charge concentration ($\nabla^2\rho < 0$), while the blue solid lines indicate the areas of charge depletion ($\nabla^2\rho > 0$). The bond critical points identified between two beryllium atoms with negative Laplacian values ($\nabla^2\rho_{\text{cp}} = -0.1176$ in BeBeNCCH_3 , -0.1079 in CNBeBeCH_3) support the formation of a real Be–Be bond, which exhibits covalent character. The negative values of the electronic energy density, $E(r)$, as -0.3154 and -0.3997 in Table S10, also stand for the interactions with significant covalent character. All Be–N interactions present a positive bond critical point (BCP) value for the Laplacian $\nabla^2\rho(r)$ ($\nabla^2\rho_{\text{cp}} = 0.6479$ in BeBeNCCH_3 , 0.7387 in BeNCCH_3 , 0.6078 in CNBeBeCH_3 , and 0.6073 in CNBeCH_3), denoting their ionic character. The negative electron energy densities at BCP ($E(r) = -0.2494$ in BeBeNCCH_3 , -0.3440 in BeNCCH_3 , -0.3663 in CNBeCH_3 and -0.3788 in CNBeBeCH_3) indicate the covalent character. Thus, the Be–N bonds are covalent polar bonds with a certain degree of both covalent and ionic contributions [38]. The localized orbital locator (LOL) map is also introduced to characterize bond effects in Figure 5 and Figure S4. The LOL values of more than $0.9e$ (red regions) in Be–Be region of our products are significant larger compared with isolated Be_2 dimer. The strong electron localization indicates the aforementioned Be–Be covalent

bonds. The strength of the Be–Be bonds in our products is also clear from the HOMO molecular orbitals involving the Be₂ moiety in Figure 5. Coherently, NBO describes the Be–Be bonds as σ bonds with a population of around two electrons (Table S8). The Wiberg bond index (WBI) for the Be–Be bonds is calculated to be 0.791 in BeBeNCCH₃ and 0.966 in CNBeBeCH₃. It is worth noting that the strength of the Be–Be bond in CNBeBeCH₃ is just slightly weaker than the C–Be and N–Be bonds, the bond orders of which are 0.976 and 0.977, respectively.

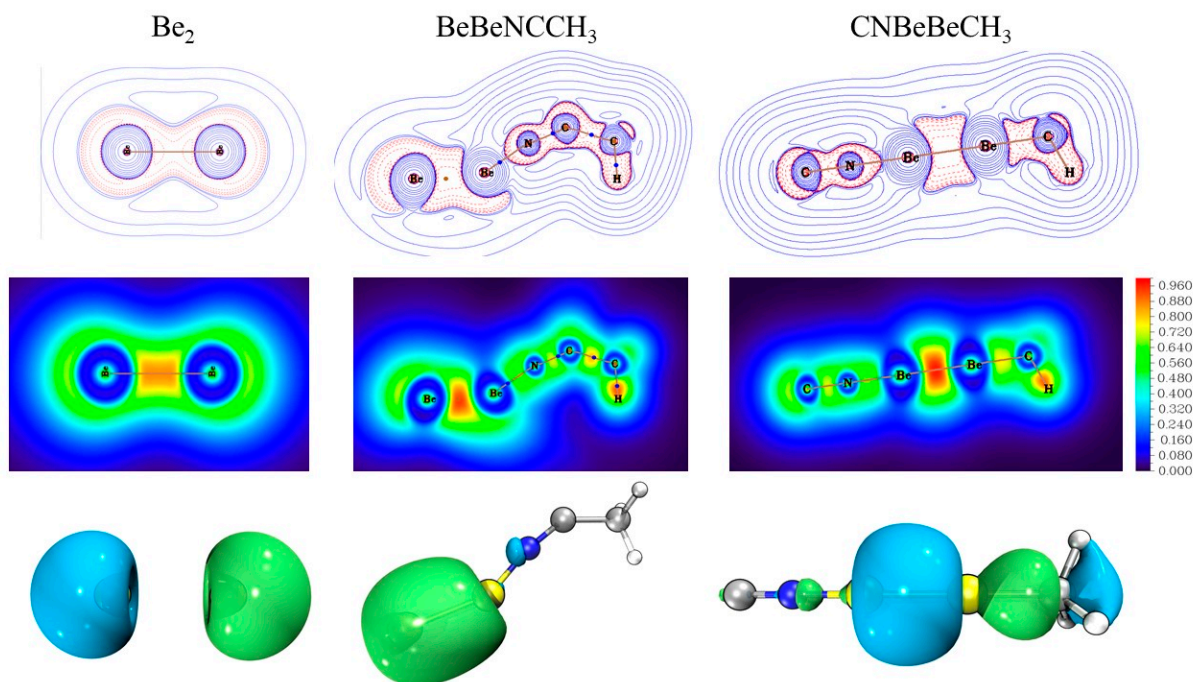


Figure 5. Contour line diagrams of the Laplacian electronic density of the diberyllium products (**first row**). Blue dots stand for BCPs. The blue solid lines and red dotted lines correspond to values of $\nabla^2\rho(r) > 0$ and $\nabla^2\rho(r) < 0$, respectively; 2D Localized Orbital Locator (LOL) map of the diberyllium products (**second row**). The HOMO molecular orbitals involving the Be₂ moiety (**last row**). The length unit is Bohr for Laplacian and LOL map.

For HBeCH₂NC, the C–C and C–N bond distances are calculated to be 1.449 and 1.153 Å, respectively. After Be–H moiety transferring from CH₂ to the N-end, the C–C bond is sizably shortened to 1.314 Å while the C–N bond is weakened (WBI from 2.923 to 1.924). The Wiberg bond order gives values of 0.985 and 1.825 for the C–C bonds of HBeCH₂CN and HBeNCCH₂, indicating single and double bonds, respectively.

4. Reaction Mechanism

The calculated reaction paths including energies of products and transition states at the CCSD(T)/B3LYP–D3/aug–cc–pVTZ level of theory are illustrated in Figure 6. The reactions of beryllium atoms with acetonitrile in excess neon can be divided into three separate paths. For all products both singlet and triplet states are considered; unless noted, the following discussion relates to the lower energy singlet state species.

The calculations indicate that beryllium dimer reacts with acetonitrile on co-deposition to form the initial structure, BeBeNCCH₃. The diberyllium end-on complex is more stable in the singlet (¹A') electronic state by exothermic 13.6 kcal/mol. BeBeNCCH₃ is also possible to be formed by adding another beryllium atom to the mono beryllium end-on complex in our experiments. The next step is both beryllium atoms bonding to the N atom to form a triangle intermediate (not observed), and an energetic barrier of 15.2 kcal/mol needs to be overcome. It later transfers to another energetically much lower cyclic intermediate

via one beryllium atom bonding to the C atom by exothermic 45.9 kcal/mol. The infrared absorptions of this cyclic intermediate are calculated and showed in Table S7. Unfortunately, its main absorptions (1609.8, 1095.5 and 768.1 cm^{-1}) are all close to the extremely strong bands of water or precursor, so we cannot make sure whether it existed in our experiment or not. The last energy barrier of insertion into the C–N bond is pretty high with 67.8 kcal/mol, and the most stable diberyllium product CNBeBeCH_3 is finally generated.

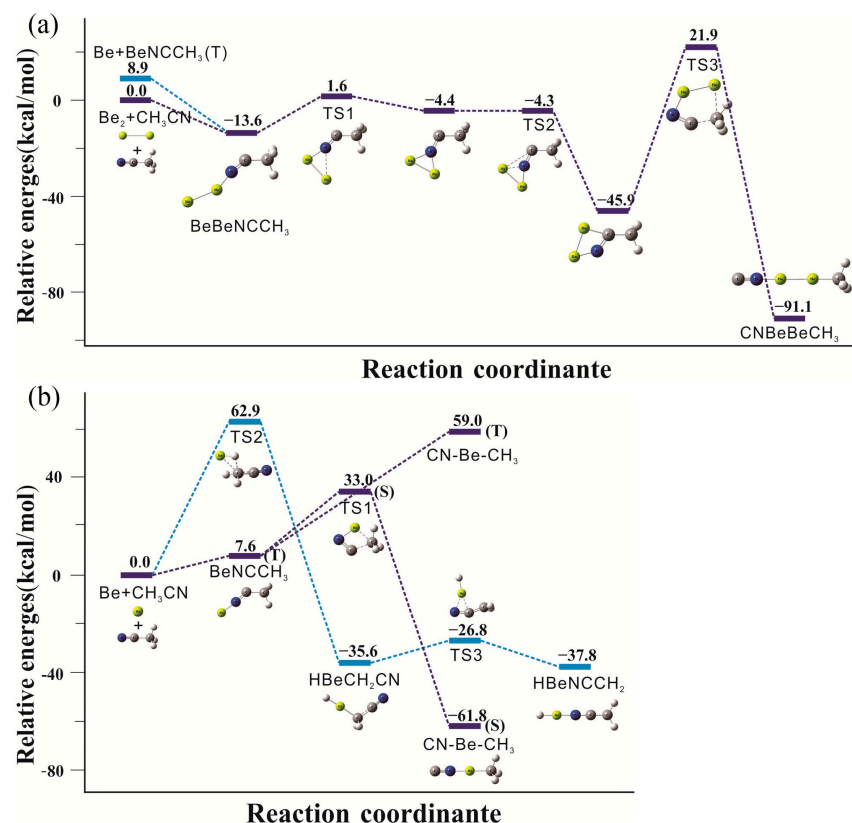


Figure 6. Calculated reaction paths in relation to the reactants [$\text{Be}/\text{Be}_2 + \text{CH}_3\text{CN}$]. (a) diberyllium reaction paths; (b) mono beryllium reaction paths. Relative energies are given in kcal mol^{-1} . S and T denote singlet and triplet electronic states, respectively.

For the mono beryllium reactions, calculations suggest that the initial end-on complex BeNCCH_3 is more stable in the triplet state, and the laser power in our experiments is able to initiate this N-coordination process. The CNBeCH_3 complex is calculated to be the global minimum for the mono beryllium products as 61.8 kcal/mol exothermic. The insertion process occurs in a single step involving the breaking of C–C bond and the formation of a new C–Be bond, which only requires to cross an energy barrier of 25.4 kcal/mol. The insertion reaction is also the primary reaction according to the strongest infrared absorptions of the product “4” after full arc irradiation. The C–H bond insertion products of acetonitrile in cryogenic matrix experiment were first observed in our experiment. The C–H insertion reaction proceeded with a high energetic cost of 62.9 kcal/mol, which was apparently supplied by photon energy during full arc photolysis, and in line with the experimental observation of HBeCH_2CN and HBeNCCH_2 only after full arc irradiation. The HBeCH_2CN complex is found to be 35.6 kcal/mol more stable than the reactants. The next step involves a relatively low energy barrier of 8.8 kcal/mol to obtain the more stable product, HBeNCCH_2 , which is exothermic by 37.8 kcal/mol.

5. Experimental and Computational Methods

The experimental details in conjunction with matrix infrared spectroscopy investigation have been described previously [39–42]. Briefly, the Nd:YAG laser fundamental

(1064 nm, 10 Hz repetition rate with 10 ns pulse width) was focused onto a rotating beryllium metal target (Alfa Aesar, Haverhill, MA, USA), and the ablated beryllium atoms were co-deposited with the gas mixture of neon and acetonitrile (Sinopharm Chemical Reagent Co., Ltd., Shanghai, China) onto a substrate (CsI) maintained at 4 K using a closed-cycle helium refrigerator (Sumitomo Heavy Industries Model RDK 205D, Tokyo, Japan) for normally 60 min. Matrix samples then were annealed and subjected to LED lights or a high-pressure mercury arc lamp (Philips, 175 W, Beijing, China) with the globe removed, and the products were confirmed by IR spectra recorded on a Bruker 80 V spectrometer in the range from 400 to 4000 cm^{-1} at 0.5 cm^{-1} resolution. The experiments were repeated using CD_3CN (Sigma-Aldrich, St. Louis, MO, USA) and $^{13}\text{CH}_3^{13}\text{CN}$ (Cambridge Isotope Laboratories, Cambridge, Britain) samples to further confirm our assignment of the products.

Quantum chemical calculations were carried out using the Gaussian 09 software package [43]. The geometry optimization and frequency calculations were performed using the hybrid B3LYP [44,45] functional including Grimme's D3-dispersion correction [46] with aug-cc-pVTZ [47,48] basis set employed for all atoms. The second-order vibrational perturbation theory (VPT2) was used to calculate the anharmonic values of the spectral parameters [49,50]. Geometries of products were reoptimized using the more strenuous CCSD method [51] and the single-point energy calculations were separately performed at the CCSD(T) [52–54]/aug-cc-pVTZ level with B3LYP-D3-optimized geometries. Bonding analyses were carried out considering Quantum Theory of Atoms in Molecules (AIM) [38], localized orbital locator (LOL) map [55] and Natural Bond Orbital (NBO) [56]. The AIM and LOL analyses were performed using Multiwfn code [57] and the NBO analysis was computed using the NBO 3.1 program. The Multiwfn and VMD [58] programs were applied for plots of HOMO molecular orbitals. The energy decomposition analysis (EDA) [59,60] combined with the natural orbital for chemical valence (NOCV) theory [61,62] was performed using the ADF 2020.101 program packages to analyze the interaction nature of the bonding fragments [63,64]. Uncontracted triple- ζ Slatertype orbital (STO) basis sets plus two sets of polarization functions (TZ2P) [65] were used for all elements. The scalar relativistic effects were included via the zeroth-order regular approximation (ZORA) Hamiltonian [66].

6. Conclusions

Beryllium atom reactions with CH_3CN give six new products. The diberyllium complexes BeBeNCCH_3 and CNBeBeCH_3 were found to be 30 kcal/mol more exothermic than the mono beryllium products because of the formation of the Be–Be single bonds. The calculated binding energies of the Be–Be bonds are -27.1 and -77.2 kcal/mol for BeBeNCCH_3 and CNBeBeCH_3 at CCSD(T)/aug-cc-pVTZ level of theory, respectively. In spite of the fact that Be is an electron-deficient element, the Be_2 moiety shows a distinct cationic character and the electron transfer from Be_2 antibonding orbitals to the bonding fragments strengthens the Be–Be bonds. AIM, LOL and NBO analyses confirm the existence of the covalent Be–Be bonds. EDA-NOCV analysis demonstrates clearly that the CNBeBeCH_3 complex can be seen as a result of the interaction between Be_2^{2+} and $(\text{H}_3\text{C}\cdots\text{NC})^{2-}$ anions. The bonding interactions between Be and N atoms are identified as covalent polar bonds because of the coexisting ionic and covalent characters from AIM analyses. Lower yields of HBeCH_2CN and HBeNCCH_2 have also been observed after full arc irradiation, and the double C=C and C=N bonds are formed after Be–H moiety transferring from CH_2 to the N-end. Finally, we hope the present study can further extend knowledge of the reactions and bonding investigations of beryllium complexes, and attract further theoretical and experimental research about beryllium chemistry.

Supplementary Materials: The following supporting information can be downloaded at: <https://www.mdpi.com/article/10.3390/molecules29010177/s1>, Figure S1: The Spin Density Plots of BeNCCH_3 at the B3LYP–D3/aug-cc-pVTZ Level of Theory. Figure S2: Selected frontier molecular orbitals of CNBeBeCH_3 calculated at B3LYP–D3/aug-cc-pVTZ level of theory. Figure S3: Contour line diagrams of the Laplacian of the electronic density of the mono beryllium products. Figure S4:

2D Localized Orbital Locator (LOL) map of the mono beryllium products. Table S1: Observed and Calculated Fundamental Frequencies of BeBeNCCH₃ Isotopomers in the Ground 3A' State. Table S2: Observed and Calculated Fundamental Frequencies of BeNCCH₃ Isotopomers in the Ground 3A1 State. Table S3: Observed and Calculated Fundamental Frequencies of CNBeBeCH₃ Isotopomers in the Ground 1A1 State. Table S4: Observed and Calculated Fundamental Frequencies of CNBeCH₃ Isotopomers in the Ground 1A1 State. Table S5: Observed and Calculated Fundamental Frequencies of HBeCH₂CN Isotopomers in the Ground 1A' State. Table S6: Observed and Calculated Fundamental Frequencies of HBeNCCH₂ Isotopomers in the Ground 1A1 State. Table S7: Calculated Fundamental Frequencies of the cyclic intermediate in the Ground 1A1 State. Table S8: NBO Analysis of Products Using the B3LYP–D3/ aug–cc–pVTZ Level of Theory. Table S9: EDA–NOCV Results at the B3LYP/TZ2P/ZORA Level of Theory for CNBeBeCH₃. Table S10: AIM Analysis of BeN, BeC and BeBe bonds in Products.

Author Contributions: Conceptualization, F.C. and X.W.; methodology, F.C. and X.W.; software, Z.P. and X.W.; validation, F.C., J.C. and L.C.; formal analysis, X.W.; investigation, F.C.; resources, X.W. data curation, F.C.; writing—original draft preparation, F.C.; writing—review and editing, F.C., Z.P. and X.W.; visualization, X.W.; supervision, X.W.; project administration, X.W.; funding acquisition, National Natural Science Foundation of China. All authors have read and agreed to the published version of the manuscript.

Funding: This research was funded by National Natural Science Foundation of China, grant number No. 22273066.

Data Availability Statement: Data are contained within the article and supplementary materials.

Conflicts of Interest: The authors declare no conflict of interest.

References

- Pan, S.; Jana, G.; Saha, R.; Zhao, L.L.; Chattaraj, P.K. Intriguing structural, bonding and reactivity features in some beryllium containing complexes. *Phys. Chem. Chem. Phys.* **2020**, *22*, 27476–27495. [\[CrossRef\]](#) [\[PubMed\]](#)
- Dutton, J.L.; Frenking, G. New Avenues in s-Block Chemistry: Beryllium(0) Complexes. *Angew. Chem. Int. Ed.* **2016**, *55*, 13380–13382. [\[CrossRef\]](#) [\[PubMed\]](#)
- Sutton, M.; Burastero, S.R. Beryllium chemical speciation in elemental human biological fluids. *Chem. Res. Toxicol.* **2003**, *16*, 1145–1154. [\[CrossRef\]](#) [\[PubMed\]](#)
- Puchta, R. A brighter beryllium. *Nat. Chem.* **2011**, *3*, 416. [\[CrossRef\]](#) [\[PubMed\]](#)
- Yuan, C.X.; Zhao, X.F.; Wu, Y.B.; Wang, X.T. Ultrashort Beryllium–Beryllium Distances Rivaling Those of Metal–Metal Quintuple Bonds Between Transition Metals. *Angew. Chem. Int. Ed.* **2016**, *55*, 15651–15655. [\[CrossRef\]](#) [\[PubMed\]](#)
- Kalemos, A. The nature of the chemical bond in Be₂⁺, Be₂, Be₂[−], and Be₃. *J. Chem. Phys.* **2016**, *145*, 214302. [\[CrossRef\]](#)
- Zhang, Q.N.; Li, W.L.; Zhao, L.L.; Chen, M.H.; Zhou, M.F.; Li, J.; Frenking, G. A Very Short Be–Be Distance but No Bond: Synthesis and Bonding Analysis of Ng–Be₂O₂–Ng' (Ng, Ng' = Ne, Ar, Kr, Xe). *Chem.-Eur. J.* **2017**, *23*, 2035–2039. [\[CrossRef\]](#)
- Patkowski, K.; Spirko, V.; Szalewicz, K. On the Elusive Twelfth Vibrational State of Beryllium Dimer. *Science* **2009**, *326*, 1382–1384. [\[CrossRef\]](#)
- Merritt, J.M.; Bondybey, V.E.; Heaven, M.C. Beryllium Dimer–Caught in the Act of Bonding. *Science* **2009**, *324*, 1548–1551. [\[CrossRef\]](#)
- Bondybey, V.E. Electronic-Structure and Bonding of Be₂. *Chem. Phys. Lett.* **1984**, *109*, 436–441. [\[CrossRef\]](#)
- Qin, Z.Z.; Wang, Q.; Yuan, C.X.; Yang, Y.T.; Zhao, X.F.; Li, D.B.; Liu, P.; Wu, Y.B. Combining covalent bonding and electrostatic attraction to achieve highly viable species with ultrashort beryllium–beryllium distances: A computational design. *Dalton Trans.* **2018**, *47*, 4707–4713. [\[CrossRef\]](#) [\[PubMed\]](#)
- Nijesh, K.; De, S.; Parameswaran, P. Homopolar dihydrogen bonding in ligand stabilized diberyllium hydride complexes, Be₂(CH₃)₂H₂L₂ (L = H[−], CO, N-heterocyclic carbene and CN[−]). *Dalton Trans.* **2016**, *45*, 7836–7846. [\[CrossRef\]](#) [\[PubMed\]](#)
- Zhang, Q.N.; Jerabek, P.; Chen, M.H.; Zhou, M.; Frenking, G. The Oxygen-Rich Beryllium Oxides BeO₄ and BeO₆. *Angew. Chem. Int. Ed.* **2016**, *55*, 10863–10867. [\[CrossRef\]](#) [\[PubMed\]](#)
- Andrews, L.; Tague, T.J.; Kushto, G.P.; Davy, R.D. Infrared-Spectra of Beryllium Carbonyls from Reactions of Beryllium Atoms with Carbon-Monoxide in Solid Argon. *Inorg. Chem.* **1995**, *34*, 2952–2961. [\[CrossRef\]](#)
- Liu, X.M.; Zhang, M.; Yu, S.; Geng, Y.; Zhang, X.X.; Ding, Y.H.; Su, Z.M. Beryllium–beryllium double-pi bonds in the octahedral cluster of Be₂(μ₂-X)₄ (X = Li, Cu, BeF). *Phys. Chem. Chem. Phys.* **2018**, *20*, 23898–23902. [\[CrossRef\]](#) [\[PubMed\]](#)
- Cui, Z.H.; Yang, W.S.; Zhao, L.L.; Ding, Y.H.; Frenking, G. Unusually Short Be–Be Distances with and without a Bond in Be₂F₂ and in the Molecular Discs Be₂B₈ and Be₂B₇[−]. *Angew. Chem. Int. Ed.* **2016**, *55*, 7841–7846. [\[CrossRef\]](#)
- Brea, O.; Corral, I. Super Strong Be–Be Bonds: Theoretical Insight into the Electronic Structure of Be–Be Complexes with Radical Ligands. *J. Phys. Chem. A* **2018**, *122*, 2258–2265. [\[CrossRef\]](#)

18. Boronski, J.T.; Crumpton, A.E.; Wales, L.L.; Aldridge, S. Diberyllocene, a stable compound of Be(I) with a Be-Be bond. *Science* **2023**, *380*, 1147–1149. [\[CrossRef\]](#)
19. West, T. The elusive Be–Be bond. *Nat. Synth* **2023**, *2*, 696. [\[CrossRef\]](#)
20. Li, X.Y.; Huo, S.H.; Zeng, Y.L.; Sun, Z.; Zheng, S.J.; Meng, L.P. Metal-Metal and Metal-Ligand Bonds in $(\eta^5\text{-C}_5\text{H}_5)_2\text{M}_2$ (M = Be, Mg, Ca, Ni, Cu, Zn). *Organometallics* **2013**, *32*, 1060–1066. [\[CrossRef\]](#)
21. Wu, S.L.; Su, J.H.; Lu, Y.; Chen, B.W.; Huang, C.Y.; Wen, Z.H.; Kuo, Y.H.; Sheu, J.H. Simplexins J-O, Eunicellin-Based Diterpenoids from a Dongsha Atoll Soft Coral *Klyxum simplex*. *B Chem. Soc. Jpn.* **2011**, *84*, 626–632. [\[CrossRef\]](#)
22. Vos, E.; Montero-Campillo, M.M.; Corral, I.; Yanez, M.; Alkorta, I.; Elguero, J. From Very Strong to Inexistent Be-Be Bonds in the Interactions of Be₂ with pi-Systems. *ChemPhysChem* **2020**, *21*, 2701–2708. [\[CrossRef\]](#) [\[PubMed\]](#)
23. Rezaie, F.; Noorizadeh, S. Strong Be-Be bonds in double-aromatic bridged Be₂(μ-SO) molecules. *Dalton Trans.* **2022**, *51*, 12596–12603. [\[CrossRef\]](#) [\[PubMed\]](#)
24. Liu, X.M.; Zhang, M.; Zhong, R.L.; Wu, S.X.; Liu, Y.Y.; Geng, Y.; Su, Z.M. Computational Study of sp_x (x = 1–3)-Hybridized Be-Be Bonds Stabilized by Amidinate Ligands. *Chem.-Eur. J.* **2020**, *26*, 10891–10895. [\[CrossRef\]](#) [\[PubMed\]](#)
25. Sarmah, K.; Kalita, A.J.; Guha, A.K. A theoretical investigation of Zn-Zn and Be-Be one electron bond. *Int. J. Quantum Chem.* **2023**, *123*, e27006. [\[CrossRef\]](#)
26. Rohman, S.S.; Kashyap, C.; Ullah, S.S.; Guha, A.K.; Mazumder, L.J.; Sharma, P.K. Ultra-Weak Metal-Metal Bonding: Is There a Beryllium-Beryllium Triple Bond? *ChemPhysChem* **2019**, *20*, 516–518. [\[CrossRef\]](#)
27. Liu, X.M.; Zhong, R.L.; Zhang, M.; Wu, S.X.; Geng, Y.; Su, Z.M. Be≡Be triple bond in Be₂X₄Y₂ clusters (X = Li, Na and Y = Li, Na, K) and a perfect classical Be≡Be triple bond presented in Be₂Na₄K₂. *Dalton Trans.* **2019**, *48*, 14590–14594. [\[CrossRef\]](#)
28. Saha, R.; Pan, S.; Merino, G.; Chattaraj, P.K. Unprecedented Bonding Situation in Viable E₂(NHB^{Me})₂ (E = Be, Mg; NHB^{Me} = (HCN^{Me})₂B) Complexes: Neutral E₂ Forms a Single E-E Covalent Bond. *Angew. Chem. Int. Ed.* **2019**, *58*, 8372–8377. [\[CrossRef\]](#)
29. Couchman, S.A.; Holzmann, N.; Frenking, G.; Wilson, D.J.D.; Dutton, J.L. Beryllium chemistry the safe way: A theoretical evaluation of low oxidation state beryllium compounds. *Dalton Trans.* **2013**, *42*, 11375–11384. [\[CrossRef\]](#)
30. Cho, H.G.; Andrews, L. Infrared spectra and density functional calculations of the M←NCCCH₃, M-η²-(NC)-CH₃, CH₃-MNC, CH₂=M(H)NC, and CH≡M(H)₂NC complexes produced by reactions of Group 6 metal atoms with acetonitrile. *J. Organomet. Chem.* **2012**, *703*, 25–33. [\[CrossRef\]](#)
31. Cho, H.G.; Andrews, L. IR Spectra and DFT Calculations of M-η²-(NC)-CH₃, CH₃-MNC, and CH₂=M(H)NC Prepared by Reactions of Laser-Ablated Hf and Ti Atoms with Acetonitrile. *Eur. J. Inorg. Chem.* **2015**, *2015*, 4379–4387. [\[CrossRef\]](#)
32. Cho, H.G.; Andrews, L. Infrared Spectra of the Complexes Os←NCCCH₃, Re←NCCCH₃, CH₃-ReNC, CH₂=Re(H)NC, and CH≡Re(H)₂NC and their Mn Counterparts Prepared by Reactions of Laser-Ablated Os, Re, and Mn Atoms with Acetonitrile in Excess Argon. *Organometallics* **2012**, *31*, 6095–6105. [\[CrossRef\]](#)
33. Cho, H.G.; Andrews, L. Infrared Spectra of CH₂=M(H)NC, CH₃-MNC, and M-η²-(NC)-CH₃ Produced by Reactions of Laser-Ablated Group 5 Metal Atoms with Acetonitrile. *J. Phys. Chem. A* **2010**, *114*, 5997–6006. [\[CrossRef\]](#) [\[PubMed\]](#)
34. Cho, H.G.; Andrews, L. Infrared Spectra of CH₂=Zr(H)NC, CH₃-ZrNC, and Zr-η²-(NC)-CH₃ Produced by Reactions of Laser-Ablated Zr Atoms with Acetonitrile. *J. Phys. Chem. A* **2010**, *114*, 891–897. [\[CrossRef\]](#) [\[PubMed\]](#)
35. Cho, H.G.; Andrews, L. Infrared Spectra of CH₃CN→M, M-η²-(NC)-CH₃, CH₃-MNC Prepared by Reactions of Laser-Ablated Fe, Ru, and Pt Atoms with Acetonitrile in Excess Argon. *Inorg. Chem.* **2019**, *58*, 16194–16204. [\[CrossRef\]](#) [\[PubMed\]](#)
36. Cho, H.G.; Andrews, L. Infrared Spectra of the M-η²-(NC)-CH₃, CH₃-MNC, and CH₂=M(H)NC Complexes Prepared by Reactions of Thorium and Uranium Atoms with Acetonitrile. *Organometallics* **2012**, *31*, 535–544. [\[CrossRef\]](#)
37. Cong, F.; Cheng, J.J.; Cho, H.G.; Huang, T.F.; Wang, X.F.; Andrews, L. M←NCCCH₃, M-η²-(NC)-CH₃, and CN–M–CH₃ Prepared by Reactions of Ce, Sm, Eu, and Lu Atoms with Acetonitrile: Matrix Infrared Spectra and Theoretical Calculations. *Inorg. Chem.* **2021**, *60*, 17649–17656. [\[CrossRef\]](#)
38. Bader, R.F.W. Atoms in Molecules. *Acc. Chem. Res.* **1985**, *18*, 9–15. [\[CrossRef\]](#)
39. Cong, F.; Cai, L.Y.; Cheng, J.J.; Wang, X.F.; Andrews, L. Boron-Mediated C–C and C–N Bond Cleavage of Acetonitrile: Matrix Infrared Spectra and Theoretical Calculations. *Organometallics* **2023**, *42*, 995–1004. [\[CrossRef\]](#)
40. Huang, T.F.; Yu, W.J.; Cheng, J.J.; Cong, F.; Xu, B.; Wang, X.F. CO₂ activation by ligand-free manganese hydrides in a parahydrogen matrix. *Chem. Commun.* **2021**, *57*, 2301–2304. [\[CrossRef\]](#)
41. Xu, B.; Beckers, H.; Ye, H.Y.; Lu, Y.; Cheng, J.J.; Wang, X.F.; Riedel, S. Cleavage of the N≡N Triple Bond and Unpredicted Formation of the Cyclic 1,3-Diaza-2,4-Diborete (FB)₂N₂ from N₂ and Fluoroborylene BF. *Angew. Chem. Int. Ed.* **2021**, *60*, 17205–17210. [\[CrossRef\]](#) [\[PubMed\]](#)
42. Cheng, J.J.; Cai, L.Y.; Cong, F.; Qiu, R.Z.; Pan, C.W.; Xu, B.; Wang, X.F. Complex with Linear B–B–B Skeleton Trapped in Dinitrogen Matrix: Matrix Infrared Spectra and Quantum Chemical Calculations. *Inorg. Chem.* **2023**, *62*, 6314–6322. [\[CrossRef\]](#) [\[PubMed\]](#)
43. Frisch, M.J.; Trucks, G.W.; Schlegel, H.B.; Scuseria, G.E.; Robb, M.A.; Cheeseman, J.R.; Scalmani, G.; Barone, V.; Mennucci, B.; Petersson, G.A. *Gaussian 09, Revision A.02*; Gaussian, Inc.: Wallingford, CT, USA, 2009.
44. Becke, A.D. Density-Functional Thermochemistry. 3. The Role of Exact Exchange. *J. Chem. Phys.* **1993**, *98*, 5648–5652. [\[CrossRef\]](#)
45. Lee, C.T.; Yang, W.T.; Parr, R.G. Development of the Colle-Salvetti Correlation-Energy Formula into a Functional of the Electron-Density. *Phys. Rev. B* **1988**, *37*, 785–789. [\[CrossRef\]](#) [\[PubMed\]](#)
46. Grimme, S.; Antony, J.; Ehrlich, S.; Krieg, H. A consistent and accurate ab initio parametrization of density functional dispersion correction (DFT-D) for the 94 elements H–Pu. *J. Chem. Phys.* **2010**, *132*, 154104. [\[CrossRef\]](#) [\[PubMed\]](#)

47. Dunning, T.H. Gaussian-Basis Sets for Use in Correlated Molecular Calculations. 1. The Atoms Boron through Neon and Hydrogen. *J. Chem. Phys.* **1989**, *90*, 1007–1023. [\[CrossRef\]](#)
48. Kendall, R.A.; Dunning, T.H.; Harrison, R.J. Electron-Affinities of the 1st-Row Atoms Revisited—Systematic Basis-Sets and Wave-Functions. *J. Chem. Phys.* **1992**, *96*, 6796–6806. [\[CrossRef\]](#)
49. Bloino, J. A VPT2 Route to Near-Infrared Spectroscopy: The Role of Mechanical and Electrical Anharmonicity. *J. Phys. Chem. A* **2015**, *119*, 5269–5287. [\[CrossRef\]](#)
50. Barone, V. Anharmonic vibrational properties by a fully automated second-order perturbative approach. *J. Chem. Phys.* **2005**, *122*, 014108. [\[CrossRef\]](#)
51. Scuseria, G.E.; Schaefer, H.F. The Unimolecular Triple Dissociation of Glyoxal—Transition-State Structures Optimized by Configuration-Interaction and Coupled Cluster-Methods. *J. Am. Chem. Soc.* **1989**, *111*, 7761–7765. [\[CrossRef\]](#)
52. Bartlett, R.J.; Musial, M. Coupled-cluster theory in quantum chemistry. *Rev. Mod. Phys.* **2007**, *79*, 291–352. [\[CrossRef\]](#)
53. Raghavachari, K.; Trucks, G.W.; Pople, J.A.; Headgordon, M. A 5th-Order Perturbation Comparison of Electron Correlation Theories. *Chem. Phys. Lett.* **1989**, *157*, 479–483. [\[CrossRef\]](#)
54. Purvis, G.D.; Bartlett, R.J. A Full Coupled-Cluster Singles and Doubles Model—The Inclusion of Disconnected Triples. *J. Chem. Phys.* **1982**, *76*, 1910–1918. [\[CrossRef\]](#)
55. Schmider, H.L.; Becke, A.D. Chemical content of the kinetic energy density. *J. Mol. Struct. THEOCHEM* **2000**, *527*, 51–61. [\[CrossRef\]](#)
56. Reed, A.E.; Curtiss, L.A.; Weinhold, F. Intermolecular Interactions from a Natural Bond Orbital, Donor-Acceptor Viewpoint. *Chem. Rev.* **1988**, *88*, 899–926. [\[CrossRef\]](#)
57. Lu, T.; Chen, F.W. Multiwfn: A multifunctional wavefunction analyzer. *J. Comput. Chem.* **2012**, *33*, 580–592. [\[CrossRef\]](#) [\[PubMed\]](#)
58. Humphrey, W.; Dalke, A.; Schulten, K. VMD: Visual molecular dynamics. *J. Mol. Graph. Model* **1996**, *14*, 33–38. [\[CrossRef\]](#)
59. Zhao, L.L.; von Hopffgarten, M.; Andrada, D.M.; Frenking, G. Energy decomposition analysis. *Wires Comput. Mol. Sci.* **2018**, *8*, e1345. [\[CrossRef\]](#)
60. Mitoraj, M.P.; Michalak, A.; Ziegler, T. A Combined Charge and Energy Decomposition Scheme for Bond Analysis. *J. Chem. Theory Comput.* **2009**, *5*, 962–975. [\[CrossRef\]](#)
61. Mitoraj, M.; Michalak, A. Natural orbitals for chemical valence as descriptors of chemical bonding in transition metal complexes. *J. Mol. Model* **2007**, *13*, 347–355. [\[CrossRef\]](#)
62. Mitoraj, M.; Michalak, A. Applications of natural orbitals for chemical valence in a description of bonding in conjugated molecules. *J. Mol. Model* **2008**, *14*, 681–687. [\[CrossRef\]](#) [\[PubMed\]](#)
63. Te Velde, G.; Bickelhaupt, F.M.; Baerends, E.J.; Guerra, C.F.; Van Gisbergen, S.J.A.; Snijders, J.G.; Ziegler, T. Chemistry with ADF. *J. Comput. Chem.* **2001**, *22*, 931–967. [\[CrossRef\]](#)
64. Baerends, E.J.; Ziegler, T.; Autschbach, J.; Bashford, D.; Bérces, A.; Bickelhaupt, F.M.; Bo, C.; Boerrigter, P.M.; Cavallo, L.; Chong, D.P.; et al. ADF2020.101, SCM, Theoretical Chemistry, Vrije Universiteit, Amsterdam, The Netherlands 2020. Available online: <http://www.scm.com> (accessed on 1 June 2023).
65. Van Lenthe, E.; Baerends, E.J. Optimized slater-type basis sets for the elements 1–118. *J. Comput. Chem.* **2003**, *24*, 1142–1156. [\[CrossRef\]](#) [\[PubMed\]](#)
66. Van Lenthe, E.; Baerends, E.J.; Snijders, J.G. Relativistic Regular Two-Component Hamiltonians Relativistic Regular Two Component Hamiltonians. *J. Chem. Phys.* **1993**, *99*, 4597–4610. [\[CrossRef\]](#)

Disclaimer/Publisher’s Note: The statements, opinions and data contained in all publications are solely those of the individual author(s) and contributor(s) and not of MDPI and/or the editor(s). MDPI and/or the editor(s) disclaim responsibility for any injury to people or property resulting from any ideas, methods, instructions or products referred to in the content.